Received: 11 February 2025 | Revised: 6 August 2025 | Accepted: 21 September 2025

DOI: 10.1111/jace.70296

Journal of the American Ceramic Society

RESEARCH ARTICLE

Defect compensation as a strategic approach to enhance photocatalytic water splitting performance of $SrTiO_3$

Mingyi Zhang | **Paul A. Salvador** | **Gregory S. Rohrer**

Department of Materials Science and Engineering, Carnegie Mellon University, Pittsburgh, Pennsylvania, USA

Correspondence
Department of Materials Science and Engineering, Carnegie Mellon University, Pittsburgh, PA 15213.
Email: gr20@andrew.cmu.edu

Funding information
National Science Foundation DMR, Grant/Award Number: 2016267; Materials Characterization Facility at Carnegie Mellon University, Grant/Award Number: 677785

Abstract

Determining suitable dopants with optimized doping concentration is critical to design efficient water splitting photocatalysts. However, there is currently a lack of fundamental knowledge to guide this process. Herein, we examine the impact of Al^{3+}, Mg^{2+}, and Ga^{3+} on the photocatalytic performance of $SrTiO_3$ and propose a defect compensation model to understand the doping effect. Doped $SrTiO_3$ crystals were grown hydrothermally and treated in molten $SrCl_2$. The hydrogen production rates from 50 catalysts produced in this way were measured with a high-throughput parallelized and automated photochemical reactor (PAPCR). The investigation revealed that all three dopants significantly enhance the photocatalytic reactivity. According to Brouwer diagrams computed using available reaction constants, the optimum reactivity is achieved when the concentration of acceptor dopants fully compensates the oxygen vacancy donors. The improved reactivity can be attributed to the reduction in free electron concentration, resulting in a space charge layer that is 1000 times longer. Consequently, this situation enhances the number of photogenerated charge carriers capable of being separated by the band bending and transported to the surface.

KEYWORDS
dopants/doping, electroceramics, photocatalysis, strontium titanate

1 | INTRODUCTION

Semiconductor based photocatalysis presents a promising approach for generating solar fuels by directly converting water into hydrogen and oxygen under illumination.[1–3] One widely employed method to improve catalyst performance is to introduce foreign ions into the host material, referred to here as doping.[4] Doping offers various advantages, including the modification of the crystal defect structure, reduction in the concentration of recombination centers, and increase in the charge carrier lifetime.[5–8] Takata et al. demonstrated that doping $SrTiO_3$ with a lower valence cation could modify the defect structure and enhance its photocatalytic reactivity.[9] Similarly, Sakata et al. doped numerous divalent cations into Ga_2O_3 and observed that Zn^{2+} contributed to a remarkable efficiency for water splitting, attributed to the increased hole concentration.[10] Doping has also been reported to sensitize wide band gap materials, enabling a response to visible light.[4] For example, the co-doing of iridium ions and alkaline earth metal ions into $NaNbO_3$ and $NaTaO_3$ contributes to their photocatalytic reactivity in the visible light region.[11] Kim et al. found that the substitution of Pb^{2+} into layered perovskites contributes to visible light sensitization

for these ultraviolet (UV)-active materials.[12] Furthermore, a Rh-doped $SrTiO_3$ photocatalyst loaded with a Pt cocatalyst has been reported to achieve a quantum yield of 5.2% at 420 nm for H_2 evolution in aqueous methanol solutions,[13] and this approach has been confirmed to work for $CaTiO_3$ as well.[14]

The discovery of a suitable dopant is important, but equally critical is the optimization of the doping level to finely tune the photocatalytic reactivity. Numerous studies provide evidence of an optimal doping concentration, wherein the photocatalytic reactivity initially increases with the doping level and then decreases. For example, Sakata et al. investigated the influence of Na^+ and determined that the addition of 2 atomic% Na to $SrTiO_3$ resulted in the most favorable reactivity.[15] Zhao et al. observed that the hydrogen production rate of Al-doped $SrTiO_3$, synthesized via a hydrothermal method, showed a dependence on Al concentration, with an optimal performance around 7.2 atom% Al as measured by X-ray fluorescence.[16] In other studies, similar observations have been reported for La-doped $NaTaO_3$,[17] Ba-doped $La_2Ti_2O_7$,[18] and Zn-doped Ga_2O_3.[10] While experimental methods commonly determine the optimal doping concentration, our current understanding of the underlying physical mechanisms remains limited. Hence, one of the primary motivations behind this study is to gain physical insight into the universal interpretation of the optimal doping concentration from the perspective of crystal defect chemistry. This insight will serve as a guide in the effective design of photocatalysts.

In this work, we examined the role of acceptor dopants on the photocatalytic reactivity of $SrTiO_3$, a model material whose defect chemistry has been thoroughly studied in past decades.[19] Al^{3+} has been recognized as an effective dopant to improve the photocatalytic performance of $SrTiO_3$.[20–23] Here, we investigated the influence of Al^{3+}, Mg^{2+}, and Ga^{3+}, as all three dopants occupy the Ti^{4+} sites and function as acceptor dopants. The catalysts were prepared with a hydrothermal approach, followed by a molten $SrCl_2$ treatment conducted in three different crucibles (Pt, Al_2O_3, and MgO). This treatment was intended to make the surface potential more anodic, thereby enhancing water oxidation activity.[20,24] $RhCrO_x$ was loaded onto the resulting crystals as a cocatalyst to enhance hydrogen evolution reaction (HER) activity and suppress surface back reactions.[25,26] The hydrogen production rates were measured with a parallelized and automated photochemical reactor (PAPCR)[27] either in pure water or in an aqueous methanol solution. Different crucibles were investigated because the crucible materials might dissolve in or otherwise react with the melt, potentially introducing unintentional dopants to the catalysts.[24,28] Our findings demonstrate that all three dopants contribute to the photocatalytic reactivity, and their impact strongly relies on both dopant concentration and the choice of crucible materials. Brouwer diagrams were generated by simulating the concentrations of point defects as a function of oxygen partial pressure. It is suggested that the introduction of Al^{3+}, Mg^{2+}, and Ga^{3+} leads to a reduction in the free electron concentration and a lowering of the Fermi level. The optimal reactivity is achieved when the oxygen vacancy donors are nearly fully compensated by acceptors, indicating a delicate balance in the doping process.

1.1 | Experimental methods

$SrTiO_3$ particles were prepared using a hydrothermal method modified from Dong et al.[29] 0.2 mL of pure $TiCl_4$ (Sigma-Aldrich, 99%) was dropped into a solution in an ice bath containing 25 mL of DI water and 1 g of ethylene glycol (Alfa Aesar, 99+%) as surfactant. The choice of the surfactant is based on our previous work showing that it yields a suitable crystal shape and size for charge separation.[30] After magnetic stirring for 5 min, 10 mL of 0.265 M $SrCl_2$ solution containing 0.42 g $SrCl_2$ (Sigma-Aldrich, 99.99%) and 30 mL of 3 M LiOH solution containing 2.16 g LiOH (Sigma-Aldrich, 98%) were added. The use of LiOH facilitates the dehydration of the $TiO_2{\cdot}nH_2O$ gel, resulting in well-defined $SrTiO_3$ crystals with sharp corners.[31] Specific amounts of $AlCl_3{\cdot}6H_2O$ (Fisher Scientific, 99%), $MgCl_2$ (Sigma-Aldrich, anhydrous, ≥98%) or $GaCl_3$ (Alfa Aesar, ultra-dry, 99.999%) were added to yield a molar ratio of x:1 with $SrTiO_3$, where x = 1%, 2%, 3%, 5%, or 10%. After stirring for another 30 min, the resulting solution was transferred to a 100 mL Teflon-lined hydrothermal autoclave (Techinstro). The autoclave was then heated at 180°C for 36 h in a furnace. After annealing, the solution was removed and the resulting precipitate was centrifugated four times at 4000 rpm for 12 min with deionized water and ethanol, respectively. Finally, the resulting precipitate was dried in an oven at 80°C overnight. To conduct the molten $SrCl_2$ treatment, 0.3 g of as prepared doped $SrTiO_3$ powders were mixed with $SrCl_2$ (Alfa Aesar, 99.5%) at a ratio of 1:10 and annealed at 1150°C in air for 10 h in an alumina crucible (Sigma-Aldrich, Coors™ high-alumina, 50 mL), a platinum crucible (Sigma-Aldrich, 30 mL), or a magnesia crucible (MSE Supplies, 30 mL) with covers. The resulting mixture was centrifugated at 4000 rpm for 18 min, four times with deionized water and another four times with ethanol, and finally dried in an oven overnight. The catalysts in this work will be denoted as "Dopant—Dopant addition—s—Crucible materials" (the -s indicates the $SrCl_2$ treatment). For example, Al3-sP represents $SrTiO_3$ samples with a 3% Al added that have been heated in a $SrCl_2$ melt in a platinum crucible.

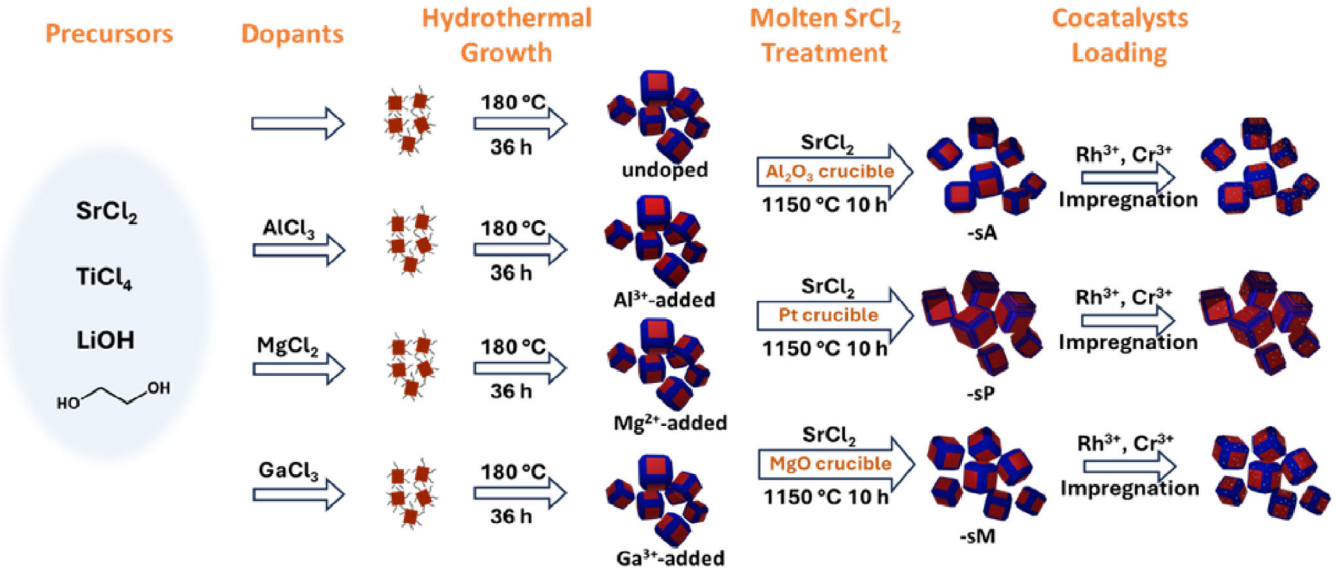

FIGURE 1 Schematic illustration of the synthesis routes for Al-doped, Mg-doped, and Ga-doped $SrTiO_3$ photocatalysts.

$RhCrO_x$ cocatalysts were deposited (0.1 wt% Rh and 0.1 wt% Cr) on all samples with an impregnation method described elsewhere.[32] Fifty milligrams of as prepared powdered samples were dispersed into 0.5 mL of deionized water containing appropriate amounts of Na_3RhCl_6 (Sigma-Aldrich) and $Cr(NO_3)_3{\cdot}6H_2O$ (Sigma-Aldrich, 99%) to yield 0.1 wt% Rh and Cr. The suspension was evaporated in a boiling water bath under constant manually stirring. The resulting powders were collected and heated at 350°C for 1 h. A schematic of the synthesis routes is shown in Figure 1.

Field Emission Scanning Electron Microscopy (FE-SEM) images were obtained to determine the morphologies of all samples using a FEI Quanta 600 with a 30 kV accelerating beam and a spot size of 3. Energy Dispersive X-ray Spectroscopy (EDS) was performed using an Oxford X-Max 80 mm SDD detector integrated with the SEM for chemical composition analysis. TEM images were recorded with a Thermal Fisher Themis 200 at 200 kV. The crystal phase was determined with powder X-ray diffraction (XRD) using an X'Pert Pro MPD X-ray diffractometer (PANalytical, Philips, The Netherlands) equipped with a high-intensity (45 kV, 40 mA) Cu K α radiation source ($K_{\alpha1}$ = 1.5406 Å, $K_{\alpha2}$ = 1.5444 Å). A scan rate of 5° min^{-1} was applied in the range of 20°–90° at a step size of 0.02°. Inductively coupled plasma optical emission spectroscopy (ICP-OES) was carried out by Element Technology to determine the dopant concentration. Photocatalytic hydrogen generation rates were measured with a high-throughput Parallelized and Automated Photochemical Reactor (PAPCR).[27,30,33] In a typical measurement, 10 mg of as prepared powders were added into a 1 mL glass vial together with 0.4 mL pH 7 DI water or 10% methanol solution with unadjusted pH. The illumination was provided by two high power 380 nm UV LED chips (Chanzon). Brouwer diagrams of Al-doped $SrTiO_3$ were plotted by simulating the concentration of the point defects using a python script modified from a code on co-doping $BaTiO_3$ developed by Ryu et al.[34,35] The code employs NumPy and SciPy packages to solve a set of defect reactions (mass conservation equation, hole trapping reaction equation, electroneutrality condition equation), as a function of oxygen partial pressure at equilibrium (high temperature) and quenched (low temperature) conditions. It employs the "brentq" method, an efficient root-finding algorithm based on Brent's method, which combines bisection, secant, and inverse quadratic interpolation for robust and fast convergence.[36] The mass-action-law parameters used in the calculations were taken from Yoo et al.[37]

2 | RESULTS

An FE-SEM image of hydrothermally prepared, undoped $SrTiO_3$ is shown in the left top panel in Figure 2A. The particles exhibit (100) and (110) facets at a suitable ratio that promotes charge separation and a diameter around 500 nm.[30,38] However, the photocatalytic reactivity of these undoped particles is below the detection limit of the PAPCR, consistent with previous work.[30] The particles were then heated in molten $SrCl_2$ in an alumina crucible, a platinum crucible, or a magnesia crucible, denoted as Undoped-sA, Undoped-sP and Undoped-sM. FE-SEM images of the $SrCl_2$ treated particles are shown in the rest of the panels in Figure 2A, showing that the crucible material

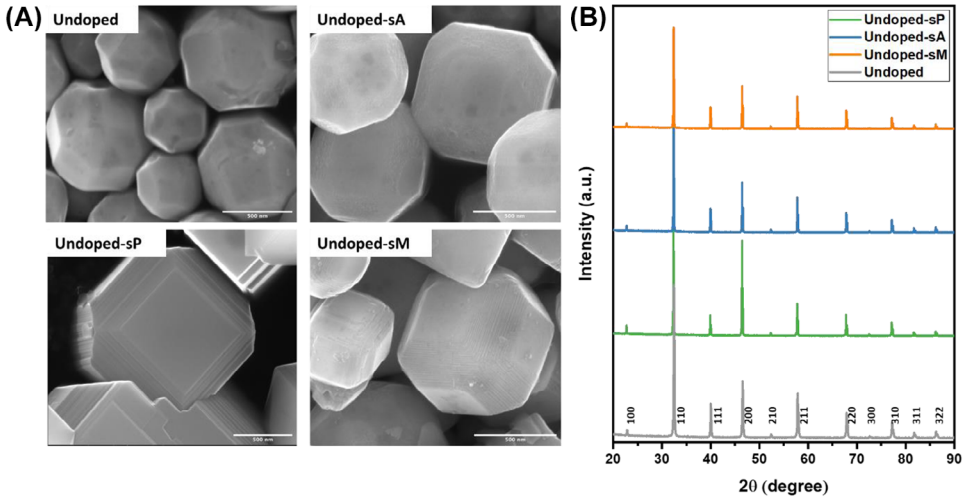

FIGURE 2 (A) FE-SEM images of hydrothermally synthesized pure $SrTiO_3$ particles, denoted as "undoped." The particles were than treated in a $SrCl_2$ melt in an alumina crucible, a platinum crucible, and a magnesia crucible, denoted as "undoped-sA," "undoped-sP," and "undoped-sM." Scale bars represent 500 nm. (B) XRD patterns of the four crystals. The peaks were indexed based on Standard patterns (ICDD: 01-073-0661).

employed in the molten $SrCl_2$ treatment leads to different particle morphologies.

Particles treated in an alumina crucible (-sA) essentially maintain their original shape (TEM images shown in Figure S1). However, the (110) facets exhibit increased roughness, and the particle edges become less defined. This phenomenon is attributed to the slight dissolution in the melt during the treatment process.[24] For particles treated in a platinum crucible (-sP), they grew much larger to several microns (though the image focuses on one of the small crystals). It is assumed that these crystals undergo coarsening in the $SrCl_2$ melt and that the shapes are the result of growth/dissolution processes. We note that the faceted structure still bounds the outer surface of the crystal with {100} and {110} planes, even though the extent of each plane is smaller. The coarsening process is assumed to be inhibited in oxide crucibles because dissolved $SrTiO_3$ can react with the crucibles rather than contribute to the growth of other particles. Particles treated in a magnesia crucible (-sM), adopt shapes that are intermediate between the last two discussed, where the (110) facets are composed of large evenly spaced straight steps along < 100 > directions. X-ray diffraction patterns of the four crystals are given in Figure 2B. All peaks are attributed to $SrTiO_3$, and no significant changes in lattice parameters are observed, consistent with previous reports.[16,20,39] Notably, after the molten $SrCl_2$ treatment, the color of some of the powder samples changed. The Undoped-sP crystals turned brown, suggesting a higher donor concentration. However, the sA and sM crystals mostly retained their white color.

Al-added $SrTiO_3$ samples were also prepared by introducing specific amounts of $AlCl_3$ along with the hydrothermal synthesis precursors to yield particles with 1% Al, 2% Al, 3% Al, 5% Al, and 10% Al added, denoted as Al1, Al2, Al3, Al5, and Al10, respectively. One must recognize that the amount of Al incorporated into the $SrTiO_3$ is unlikely to be equal to that added during the synthesis; more realistically, the actual doping concentration should increase with the dopant addition until the solubility limit is reached. Next, the crystals were treated in molten $SrCl_2$ in an alumina crucible, a platinum crucible, or a magnesia crucible, denoted as -sA, -sP, and -sM, and FE-SEM images of the resulting particles are shown in Figure 3. The particle morphologies are generally consistent with those in Figure 2. Particles treated in an alumina crucible largely retain their original shape. However, the use of a platinum crucible for the molten $SrCl_2$ treatment results in larger particles with a layered feature on the surface. Interestingly, the color of these powders gradually turns from brown to white as the Al concentration increases, suggesting a reduction in the donor concentration that would be consistent with increased acceptor compensation of oxygen vacancies. Those treated in a magnesia crucible exhibit a relatively irregular shape, exposing stepped (110) facets. The amount of Al added seems to have minimal influence on the final shape of the particles.

Photocatalytic hydrogen production rates of the 15 molten $SrCl_2$ treated Al-doped $SrTiO_3$ crystals were measured using the PAPCR in pH 7 deionized water or 10% methanol solution with an unadjusted pH. The maximum production rates were plotted in Figure 4 as a function of Al dopant addition (not the actual doping concentration). Particles treated in an alumina crucible exhibit significantly higher reactivity compared to those treated in a

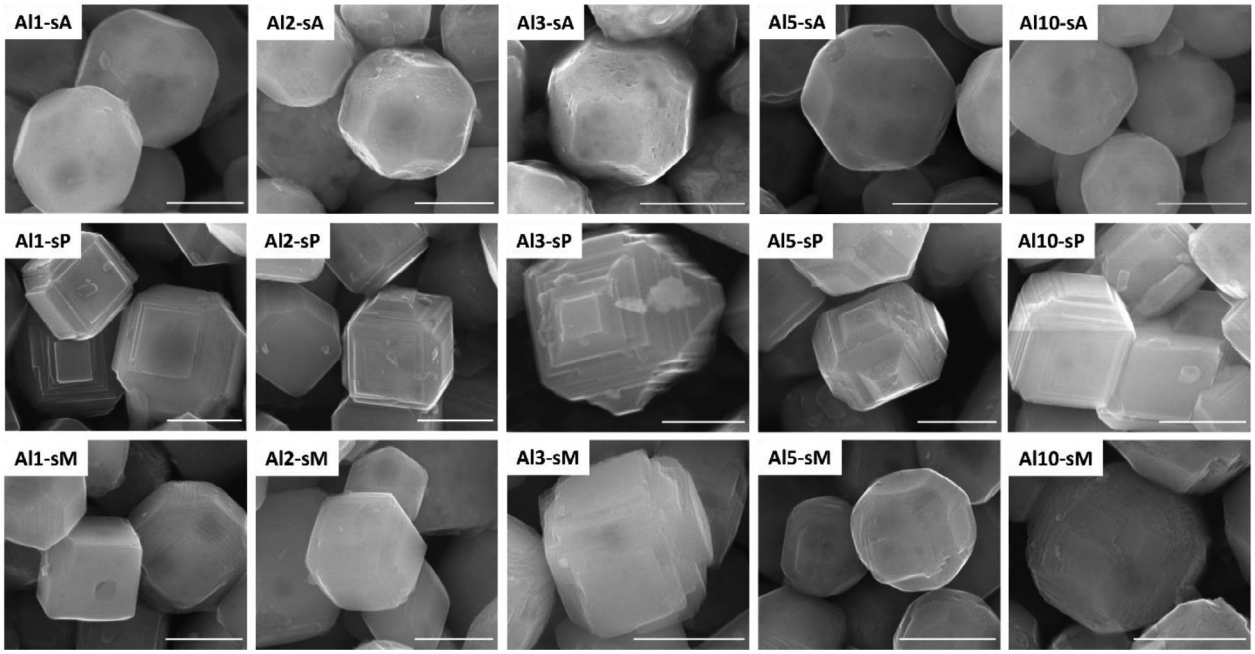

FIGURE 3 FE-SEM images of Al-added particles that have been treated in molten $SrCl_2$ in an alumina crucible (-sA), a platinum crucible (-sP), and a magnesia crucible (-sM). The numbers represent Al dopant additions. The scale bar represents 500 nm.

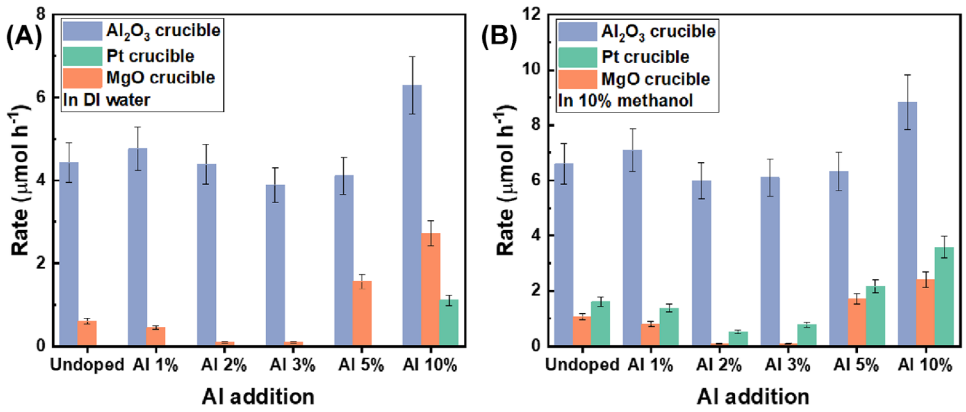

FIGURE 4 Photocatalytic maximum hydrogen production rates of Al-added $SrTiO_3$ crystals in (A) pH 7 DI water and (B) 10% methanol as a function of Al addition. The crystals have been treated in a $SrCl_2$ melt in an alumina crucible, a magnesia crucible, or a platinum crucible. The bars represent standard deviations.

platinum crucible or a magnesium crucible. The addition of Al seems to have a relatively weak effect on the reactivity when the molten salt treatment is carried out in an alumina crucible, suggesting that the crucible might be acting as an Al source that saturates the $SrTiO_3$ such that all of the catalysts have approximately the same Al concentration. This is consistent with recent reports that the $SrCl_2$ melt dissolves Al^{3+} from the crucible.[20] The molten $SrCl_2$ treatment in a platinum crucible leads to the lowest reactivity, with no detectable hydrogen production using the PAPCR until 10% Al^{3+} is introduced into the precursors. The $SrCl_2$ treatment in a magnesia crucible leads to catalysts with an intermediate reactivity, and the reactivity remains low with increasing Al^{3+} addition until a high concentration is introduced. Adding methanol as a scavenger increases the reactivity for all samples, consistent with previous reports.[30,40]

Mg-added and Ga-added $SrTiO_3$ were prepared by mixing specific amount of $MgCl_2$ or $GaCl_3$ into the precursors of the hydrothermal synthesis. Again, the dopant additions were controlled to be 1%, 2%, 3%, 5%, and 10%. FE-SEM images of the 15 Mg-added $SrTiO_3$ images are shown in Figure S2, and the particle morphologies are slightly different from the Al-added crystals. For example, Mg-added

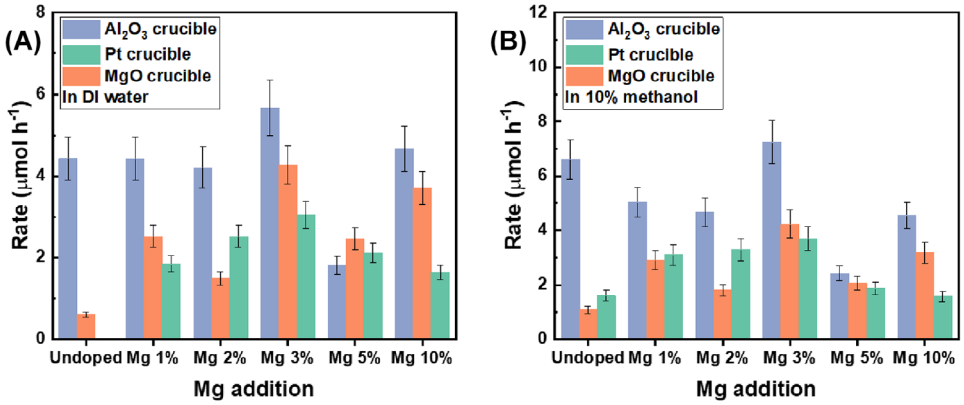

FIGURE 5 Photocatalytic maximum hydrogen production rates of Mg-added $SrTiO_3$ crystals in (A) pH 7 DI water and (B) 10% methanol as a function of Mg addition. The crystals have been treated in the molten $SrCl_2$ in an alumina crucible, a magnesia crucible, or a platinum crucible. The bars represent standard deviations.

samples treated in a platinum crucible have a layer-stacking feature, but we can still identify (110) facets in Mg1-sP and Mg2-sP. Besides, for crystals that have undergone a molten $SrCl_2$ treatment in a magnesia crucible, the (110) facets in Mg-added samples have fewer steps compared with Al-added samples. Again, those crystals that have been treated in an alumina crucible maintain the original morphology. Figure 5 shows the measured photocatalytic hydrogen production rates of the 15 Mg-added $SrTiO_3$ samples, and they generally exhibit higher reactivity compared to their Al-added counterparts (as seen in Figure 4). When the $SrCl_2$ treatment was conducted in an alumina crucible, Mg-added samples produce hydrogen at a similar level to the Al-added samples—consistent with the idea that the reactivity is determined by Al supplied by the crucible. However, in cases where the $SrCl_2$ treatment was carried out in a magnesia crucible or a platinum crucible, the Mg-added samples display significantly higher reactivity than the Al-added samples (though these are still less reactive than samples treated in alumina crucibles). Furthermore, a maximum reactivity occurs at 3 % Mg^{2+} for the samples treated in Pt or MgO crucibles. This pattern holds true for both pure water and 10% methanol solutions. The data indicate that the Al doping concentration is significantly lower than that of Mg prior to the $SrCl_2$ treatment, suggesting that hydrothermal doping is less effective for Al. In contrast, the molten $SrCl_2$ treatment in an Al_2O_3 crucible proves to be a particularly effective method for incorporating Al ions into the $SrTiO_3$ lattice.

FE-SEM images of the 15 Ga-added $SrTiO_3$ crystals that have been heated in a $SrCl_2$ melt are given in Figure S3. Their morphologies are basically the same as Al-added samples, depending on the type of crucibles for the molten salt treatment. Figure 6 illustrates the photocatalytic hydrogen production rates plotted against the Ga addition. Consistent with the results in Figures 4 and 5, samples heated in an alumina crucible yield the highest reactivity. However, for Ga-added samples treated in either a platinum crucible or a magnesia crucible, the hydrogen production rates are disappointingly low. This result indicates that the reactivity is unaffected by the amount of Ga^{3+} added during hydrothermal synthesis.

TABLE 1 Molar ratios determined by ICP-OES of selected $SrTiO_3$ crystals.

Sample	M%/(M% + Ti%)
Al1	0.044%
Mg1	0.24%
Mg3	1.01%
Ga3	0.36%
Undoped-sA	2.58%

To quantify the amount of dopant dissolved in the catalyst, ICP-OES analysis has been carried out on selected samples. A total of five samples were measured and the corresponding doping concentrations are given in Table 1. Al1, Mg1, Mg3, and Ga3 represents hydrothermal doped crystals without the $SrCl_2$ treatment. The letters represent the type of dopant added, and the numbers represent the dopant additions: 1%, 1%, 3%, and 3%. Undoped-sA corresponds to hydrothermal particles without any dopants introduced that have been treated in the molten $SrCl_2$ in an alumina crucible.

The dopant concentration of the rest of the samples were estimated using the data in Table 1, assuming that the dopant concentration is proportional to dopant addition and given in Table S1. These assumptions are grounded in the solubility limits, which are at least 1.8 mol% for Al and 10 mol% for Mg.[37,41,42] We also assume that the platinum crucible won't introduce impurities into the samples, therefore we employ the numbers in Table S1 as

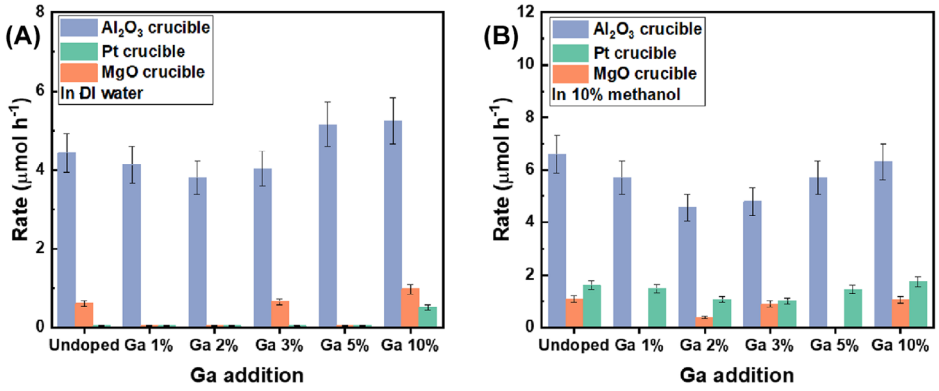

FIGURE 6 Photocatalytic maximum hydrogen production rates of Ga-added $SrTiO_3$ crystals in (A) pH 7 DI water and (B) 10% methanol as a function of Ga addition. The crystals have been treated in the molten $SrCl_2$ in an alumina crucible, a magnesia crucible, or a platinum crucible. The bars represent standard deviations.

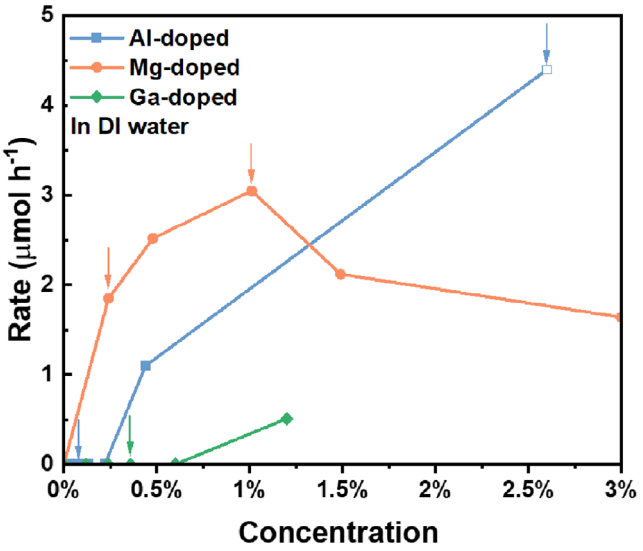

FIGURE 7 Photocatalytic maximum hydrogen production rates in DI water of Al-doped, Mg-doped, and Ga-doped $SrTiO_3$ crystals as a function of doping concentration. The undoped samples that have undergone a $SrCl_2$ treatment in an alumina crucible is plotted as an empty square. The rest of the samples have undergone a $SrCl_2$ treatment in a platinum crucible. The measured points are labeled with arrows.

the doping concentration for those samples that have been heated in a $SrCl_2$ melt in a platinum crucible (-sP). We also used EDS to confirm that the estimated doping concentrations fall within a similar range and that the materials maintain a consistent Sr/Ti ratio (Figures S4 and S5). Figure 7 presents the photocatalytic hydrogen production rates as a function of doping concentrations. To facilitate a better comparison of the influence of dopant elements and doping concentration, the data for undoped-sA, pure $SrTiO_3$ particles treated in an alumina crucible, was added to the figure as a hollow square. In the case of the molten $SrCl_2$ treatment carried out in a platinum crucible, Mg^{2+} emerges as the most favorable dopant, while Ga^{3+} exhibits the least reactivity. Notably, the three dopants have distinct optimal doping concentrations. For Al-doped samples, the hydrogen production rate rises with the doping concentration, reaching its maximum reactivity at 2.5%. Given that the photocatalytic hydrogen evolution rate remains largely unchanged despite varying Al additions during the $SrCl_2$ treatment in an Al_2O_3 crucible, we infer that Al doping has reached saturation, and the sample has achieved its maximum reactivity. However, for Mg-doped samples, the optimal reactivity is observed at 1%, considerably lower than that of the Al-doped ones. As for Ga-doped samples, it is evident that the reactivity increases with the doping concentration, but the data provided here does not confirm its optimal concentration. It is important to note that we assumed the concentration to be constant before and after the molten salt treatment in a platinum crucible. However, it is possible that the dopants might dilute or concentrate due to dissolution/precipitation in the melt or the change in oxygen vacancies.

3 | DISCUSSION

The findings clearly demonstrate that the choice of crucible materials used in the molten $SrCl_2$ treatment has a significant impact on the resulting $SrTiO_3$ crystals, affecting both their morphology, dopant content, and photocatalytic reactivities. When the Pt crucible is employed, the dissolution of $SrTiO_3$ in the melt leads to particle coarsening, as the Pt is an inert vessel. On the other hand, the $SrCl_2$ melt wets and reacts with Al_2O_3 crucibles, so that little or no $SrCl_2$ is found at the end of the heat treatment.[24] The magnesia crucibles also showed signs of erosion similar to Al_2O_3 crucibles, but this process was not studied. As a consequence, the actual contact time between $SrTiO_3$ and the melt is much shorter compared to that in Pt crucibles

and the $SrTiO_3$ can be partially consumed by the side reactions. This observation is supported by our previous work on $SrTiO_3$ single crystal substrates.[24] Another notable difference is that Al and Mg dissolve from the crucible and can be incorporated into the $SrTiO_3$ lattice, serving as dopants. In contrast, a Pt crucible is less likely to introduce impurities into $SrTiO_3$, making the crystals obtained from it more suitable for understanding the specific role of dopants.

While particle morphology is also known to affect photocatalytic reactivities, for $SrTiO_3$, (100) and (110) facets serve as cathodic and anodic reaction sites, respectively. Crystals that expose both facets are generally more reactive than those exposing only one facet type or having irregular shapes.[43,44] In our study, the choice of crucible material was found to influence crystal morphology. Compared to the as-grown crystals from hydrothermal synthesis, those treated with $SrCl_2$ in Al_2O_3 or MgO crucibles largely retained their original morphology, although slight surface etching was observed. Even though crystals from the Pt crucible experience significant morphological changes, the (110) facets transition from large to numerous smaller facets. Therefore, the overall relative areas of (100)/(110) remain comparable, despite variations in detailed structure. Thus, the primary determinant of photocatalytic performance in this context is still the defect structure associated with dopants.

Introducing cation acceptors into $SrTiO_3$ could potentially compensate oxygen vacancy donors and consequently contribute to the photocatalytic reactivity. Among the cation acceptors, Al^{3+} is considered effective for $SrTiO_3$ as it minimizes the formation of Ti^{3+} recombination centers, which are known to limit reactivity.[22] Here, Mg^{2+} and Ga^{3+} are studied along with Al^{3+} as they all occupy Ti sites.[41,45] Both Mg^{2+} and Al^{3+} share similar ionic radii, while Ga^{3+} possesses the same valence state as Al^{3+}. In the following discussion, we analyze the doping effect from the perspective of defect chemistry.

Unintentionally doped $SrTiO_3$ is known to be an n-type semiconductor because of intrinsic oxygen vacancies.[37] There might be background acceptor impurities from the source materials, such as monovalent alkali ions (Na(I) and K(I)) on the A-site and trivalent metals (Fe(III) and Al(III)) on the B-site. Because the oxygen vacancy concentration is much greater than the background impurities, especially in this experiment where we employed precursors of the highest obtainable purity in the hydrothermal synthesis, the material is overall n-type. The formation of oxygen vacancies can be expressed in Kröger–Vink notation as:

$$O_O^* \rightarrow \frac{1}{2}O_2(g) + V_O^{\cdot\cdot} + 2e' \quad (1)$$

The dissolution of Al, Mg, and Ga in $SrTiO_3$ can be written assuming ionic compensation as:[9,46]

$$2SrO + Al_2O_3 \overset{2SrTiO_3}{\rightarrow} 2Al_{Ti}' + 5O_O^* + V_O^{\cdot\cdot} + 2Sr_{Sr}^* \quad (2)$$

$$SrO + MgO \overset{SrTiO_3}{\rightarrow} Mg_{Ti}'' + 2O_O^* + V_O^{\cdot\cdot} + Sr_{Sr}^* \quad (3)$$

$$2SrO + Ga_2O_3 \overset{2SrTiO_3}{\rightarrow} 2Ga_{Ti}' + 5O_O^* + V_O^{\cdot\cdot} + 2Sr_{Sr}^* \quad (4)$$

The intrinsic electron hole pair generation and the dopant ionization reactions can be written as (note that they do not have to be fully ionized as written and the equilibrium constant varies with dopant):

$$\emptyset = e' + h^{\cdot} \quad (5)$$

$$Al_{Ti}^* = Al_{Ti}' + h^{\cdot} \quad (6)$$

$$Mg_{Ti}^* = Mg_{Ti}'' + 2h^{\cdot} \quad (7)$$

$$Ga_{Ti}^* = Ga_{Ti}' + h^{\cdot} \quad (8)$$

Here, we can see that each ionized Mg acceptor dopant (Mg_{Ti}'') can provide two positive charges, while each Al or Ga dopant can only provide one positive charge. This implies that the point of full compensation, where $n = p$, should be different for Mg^{2+} and Al^{3+} (Ga^{3+}). Mg-doped $SrTiO_3$ should reach the full compensation point at a lower doping concentration compared with Al and Ga, assuming similar ionization energies. The electroneutrality condition equations can then be written as:

$$n + [Al_{Ti}'] + [Ti_{Ti}'] = p + 2[V_O^{\cdot\cdot}] \quad (9)$$

$$n + 2[Mg_{Ti}''] + [Ti_{Ti}'] = p + 2[V_O^{\cdot\cdot}] \quad (10)$$

$$n + [Ga_{Ti}'] + [Ti_{Ti}'] = p + 2[V_O^{\cdot\cdot}] \quad (11)$$

Note the Schottky reaction is significant in $SrTiO_3$ when $T > 1500°C$.[47] Since the molten $SrCl_2$ treatment is carried out at 1150°C, the concentration of cation vacancies arising from the Schottky reaction should be negligibly low, thus we assume they can be neglected. We also ignore Equation 2 here as the equilibrium constant is not known (i.e., $[Ti_{Ti}'] \approx 0$). To simulate the defect structure, the concentrations of the point defects have been calculated for Al-doped $SrTiO_3$ using the mass-action-law parameters measured by Yoo et al:[37]

$$\emptyset = e' + h^{\cdot}$$

$$K_i/cm^{-6} = np = 6.01 \times 10^{41} \exp(-2.12\,eV/kT) \quad (12)$$

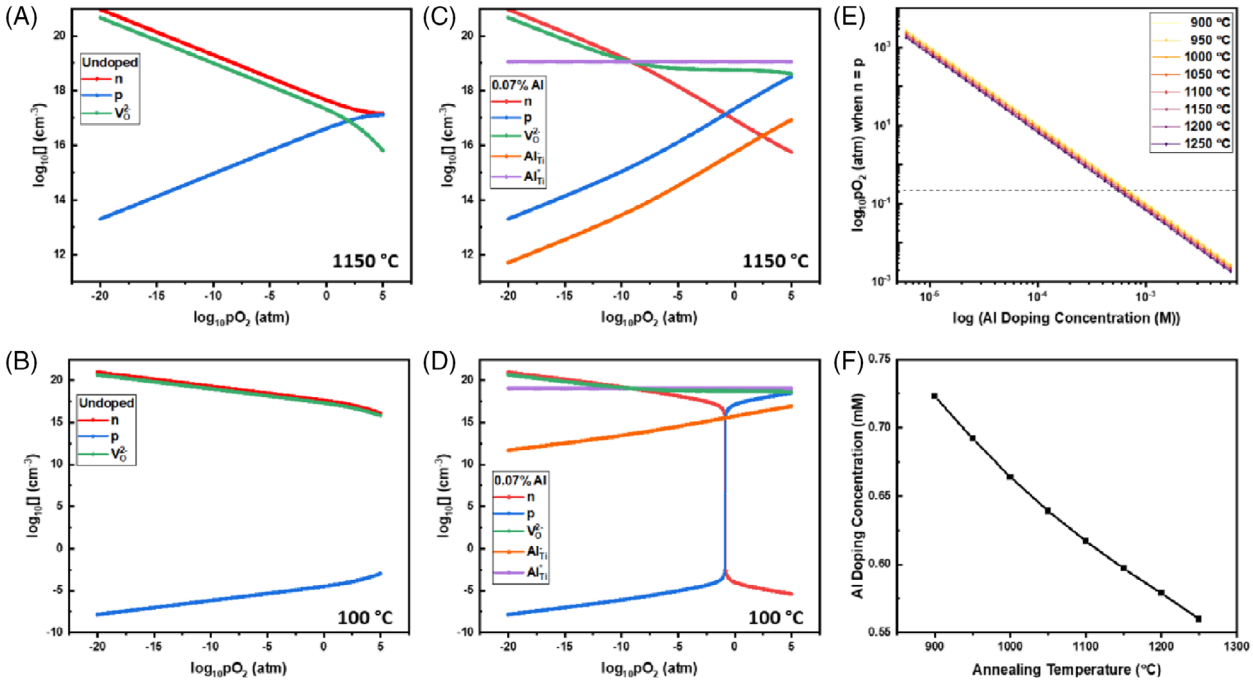

FIGURE 8 (A–D) Brouwer diagrams of undoped $SrTiO_3$ and 0.07% Al-doped $SrTiO_3$ at 1150°C and 100°C. (E) The relationship between oxygen partial pressure and Al doping concentration required for charge neutrality ($n = p$) at various annealing temperatures. (F) The Al concentration needed to achieve $n = p$ at an oxygen partial pressure of 0.21 atm across different annealing temperatures. The calculation employed a python code modified from the code on co-doping $BaTiO_3$ developed by Ryu et al.[34,35]

$$V_{\ddot{O}} + \frac{1}{2}O_2 = O_O^* + 2h^{\cdot}$$

$$K_O/cm^{-3} = p^2/\left[V_{\ddot{O}}\right] p_{O_2}^{1/2} = 6.57 \times 10^{23}\exp(-2.23\,eV/kT) \tag{13}$$

$$Al_{Ti}^* = Al_{Ti}' + h^{\cdot}$$

$$K_{Al}/cm^{-3} = \left[Al_{Ti}'\right] p/\left[Al_{Ti}^*\right] = 2.71 \times 10^{25}\exp(-1.35\,eV/kT) \tag{14}$$

Brouwer diagrams of undoped $SrTiO_3$ at 1150°C and 100°C are plotted in Figure 8A and B as a function of oxygen partial pressure. The high temperature plots describe the situation in a $SrCl_2$ melt, and the low temperature plots are close to the materials in the reactor. When oxygen partial pressure is set to 0.21 atm, the free electron concentration and hole concentration are on the order of 10^{17} cm^{-3} and 10^{16} cm^{-3} at 1150°C. After cooling the materials, the carriers will not be thermally ionized to the same degree. However, the free electron concentration needs to be similar to the oxygen vacancy concentration ($n \approx 2[V_O^{\cdot\cdot}]$) to maintain charge neutrality, so it remains on the order of 10^{17} cm^{-3}. This reduces the magnitude of the hole concentration to the order of 10^{-5} cm^{-3}. This will enhance the n-type characteristics of the materials and shift the Fermi level to a more cathodic region.

Brouwer diagrams of 0.07% Al-doped $SrTiO_3$ are given in Figure 8C and D, a doping concentration describing $[V_O^{\cdot\cdot}] \approx 2[Al_{Ti}']$. At 0.21 atm, the free electron concentration is very close to the hole concentration, meaning that the semiconductor is close to the full compensation point. After cooling the materials, at the compensation point, there will be a precipitous drop in electron concentration which has been studied by Waser et al.[48] This will significantly reduce the free electron concentration from the order of 10^{17} cm^{-3} to the order of 10^{13} cm^{-3}. Note that the Debye length of $SrTiO_3$ was estimated to be 3.2 nm, assuming a carrier concentration of 3×10^{19} cm^{-3}.[49] If the dielectric constant is conserved, the six order of magnitude decrease of the free electron concentration will then increase the Debye length and the space charge length roughly 1000 times. Note that the light penetration length is roughly 10 μm at 380 nm illumination, assuming the absorption coefficient is on the order of 100 cm^{-1}.[50] Therefore, more photogenerated charge carriers will now be generated in the space charge layer instead of the flat band region and they can be separated by the electric field induced by band bending and migrate to the surface to participate in reactions.[51–53] This will lead to a reduced charge recombination rate and a much longer charge carrier lifetime, ultimately increasing the photocatalytic reactivity. On the other hand, adding excessive dopants lowers the Fermi level and the potential difference between the semiconductor and the solution, therefore reduces the degree

of band bending, the benefit of the compensation will be lost. This explains the existence of the optimal accepter doping concentrations for photocatalytic reactions.[16,20,30] The relationship between oxygen partial pressure and Al-doping concentration was simulated across a range of annealing temperatures from 900°C to 1250°C (Figure 8E). The Al concentrations required for charge compensation ($n = p$) at 0.21 atm at various annealing temperatures are shown in Figure 8F, falling predominantly within the range of 0.055% to 0.075%. If one assumes that Mg-doped $SrTiO_3$ shares similar mass-action-law parameters, based on the ionization reactions (see Equation 7), each Mg dopant can provide more than one positive charge, suggesting that it can compensate the oxygen vacancies more efficiently. Simulated Brouwer diagrams for 0.07% Mg-doped $SrTiO_3$ are presented in Figure S6. From the data in Figure 7, the optimal concentration for Mg-doped samples is roughly one half of the doping concentration of Al-doped samples associated with the maximum reactivity, consistent with this model. The likely crystal structures and the illustrated band energy levels of Al-doped $SrTiO_3$ and Mg-doped $SrTiO_3$ are shown in Figure S7. The simulated Brouwer diagram for Ga-doped $SrTiO_3$ is not included here due to the absence of reported ionization energy values for Ga acceptors in the literature. A possible reason for the poor reactivity of Ga-doped samples is the higher ionization energy of Ga acceptors compared to Al and Mg, coupled with its lower solubility.

Some previous work supports our model from different perspectives. Zhao et al. studied the electronic structure of Al-doped $SrTiO_3$ using XPS and DFT and found that the incorporation of Al^{3+} might lower the Fermi level by approximately 0.5 eV and make the material less n-type,[22] which is consistent with our calculation of the decrease of the free electron concentration. Their simulation also shows the sensitivity of the Al locations, if two Al ions sit next to the oxygen vacancy, the band gap of the material will resemble pure $SrTiO_3$, a situation close to the fully compensated (semi-insulated) material. Besides, the decrease of free electron concentration as well as the formation of $[Al'_{Ti} - V_O^{\cdot\cdot} - Al'_{Ti}]$ will reduce the formation of Ti^{3+} traps. Cheng and Long studied Al-doped and Na-doped $SrTiO_3$ using nonadiabatic molecular dynamics, indicating that when two Ti^{4+} ions or two Sr^{2+} ions are equally replaced by Al^{3+} or Na^{+} ions, the in-gap trap state created by oxygen vacancies can be eliminated and the recombination rate was reduced.[54] Li et al. conducted photoluminescence measurements and found that the carrier lifetime in Al-doped $SrTiO_3$ increases only slightly, suggesting that improved photocatalytic performance can be primarily attributed to efficient charge separation rather than prolonged intrinsic carrier lifetimes.[55] Han et al. have studied solid state prepared Mg-doped $SrTiO_3$, suggesting that the incorporation of Mg^{2+} would expand the depletion layer from 25 to 50 nm and improve the photocatalytic reactivity.[56] Similar results have also been reported on other materials. For example, in n-type Si doped with In, as the concentration of deep acceptor levels increases in a narrow range close to the concentration of shallow donors, the electron and hole lifetimes and the photoconductivity increase by several orders of magnitude.[57]

One issue that needs to be addressed is that the optimal Al concentration measured from the experiment is obviously higher than the calculated compensation point. We believe this distinction is ascribed to the fact that the calculation is based on the mass action parameters in air rather than the $SrCl_2$ melt. Previous experiments reveal that annealing $SrTiO_3$ in molten $SrCl_2$ treatment changes the properties of the material.[24] One possible explanation is that the oxygen partial pressure is much lower in the $SrCl_2$ melt, requiring more acceptor dopants to compensate the material. This is supported by the fact that a $SrTiO_3$ single crystal substrate turned black after heating in a $SrCl_2$ melt in a platinum crucible.[24,58] Another explanation is that the defect reactions are more complex in the melt compared with that in air, such as the melt introduces $Cl_O^{\cdot}$ donors in the crystal.

It is important to mention that in our simulation, we neglected the presence of cation vacancies because the concentration produced by the Schottky reaction at this temperature is neglibible.[47] The melt provides a strontium-rich environment, which can additionally suppress the formation of strontium vacancies. However, the oxygen vacancy concentration could be higher because the melt might be more reducing than air. This hypothesis aligns with the earlier discussion concerning the depleted oxygen environment, as the concentration of oxygen vacancies is inversely proportional to the oxygen partial pressure, as shown in Figure 8. All the factors will increase the free electron concentration, which will require a greater acceptor concentration to reach the compensation point.

4 | CONCLUSION

The influences of Al^{3+}, Mg^{3+}, and Ga^{3+} acceptor dopants on the photocatalytic reactivity of $SrTiO_3$ have been studied. The findings reveal that all three dopants influenced the performance of the photocatalyst. Of equal importance was the crucible material used for the molten salt treatment; alumina crucibles led to large (2.6 %) concentrations of Al in the catalyst. We propose a model for defect compensation in which the optimal acceptor concentration is close to a situation where the oxygen vacancy donors are fully compensated, which can be simplified as $[V_O^{\cdot\cdot}] \approx 2[Al'_{Ti}]$, $[V_O^{\cdot\cdot}] \approx [Mg''_{Ti}]$, and $[V_O^{\cdot\cdot}] \approx 2[Ga'_{Ti}]$ for the three

dopants, respectively. At the compensation point, the space charge layer would expand by as much as 1000 times, so that more photogenerated charge carriers can be separated by the field and moved to the surface. The reduction of the free electron concentration associated with the formation of $[Al'_{Ti} - V_O^{\cdot\cdot} - Al'_{Ti}]$ would also lower the Fermi level and inhibit the formation of Ti^{3+} traps. Our work offers a plausible quantitative explanation on the role of acceptor dopants on $SrTiO_3$, and the principles serve as a guideline for the systematic design and optimization of various oxide photocatalysts.

ACKNOWLEDGMENTS

This work was supported by the National Science Foundation under Grant Number: DMR 2016267, and the authors acknowledge the use of the Materials Characterization Facility at Carnegie Mellon University supported by Grant Number: MCF-677785. The authors thank Dr. John R. McGarrahan and Dr. Elizabeth C. Dickey on the help of the defect structure simulation.

ORCID

Paul A. Salvador https://orcid.org/0000-0001-7106-0017
Gregory S. Rohrer https://orcid.org/0000-0002-9671-3034

REFERENCES

1. Nishioka S, Osterloh FE, Wang X, Mallouk TE, Maeda K. Photocatalytic water splitting. Nat Rev Methods Primer. 2023 Jun 1;3(1):42.
2. Gupta A, Likozar B, Jana R, Chanu WC, Singh MK. A review of hydrogen production processes by photocatalytic water splitting—from atomistic catalysis design to optimal reactor engineering. Int J Hydrog Energy. 2022;47(78):33282–307.
3. Wang Q, Domen K. Particulate photocatalysts for light-driven water splitting: mechanisms, challenges, and design strategies. Chem Rev. 2020;120(2):919–85.
4. Kudo A, Miseki Y. Heterogeneous photocatalyst materials for water splitting. Chem Soc Rev. 2009;38(1):253–78.
5. Feng Y, Wu J, Chi Q, Li W, Yu Y, Fei W. Defects and aliovalent doping engineering in electroceramics. Chem Rev. 2020 Feb 12;120(3):1710–87.
6. Bai S, Zhang N, Gao C, Xiong Y. Defect engineering in photocatalytic materials. Nano Energy. 2018;53:296–336.
7. Liu J, Wei Z, Shangguan W. Defects engineering in photocatalytic water splitting materials. ChemCatChem. 2019;11(24):6177–89.
8. Sarkar A, Khan GG. The formation and detection techniques of oxygen vacancies in titanium oxide-based nanostructures. Nanoscale. 2019;11(8):3414–44.
9. Takata T, Domen K. Defect engineering of photocatalysts by doping of aliovalent metal cations for efficient water splitting. J Phys Chem C. 2009;113(45):19386–88.
10. Sakata Y, Matsuda Y, Yanagida T, Hirata K, Imamura H, Teramura K. Effect of metal ion addition in a Ni supported Ga_2O_3 photocatalyst on the photocatalytic overall splitting of H_2O. Catal Lett. 2008;125(1):22–26.
11. Iwase A, Saito K, Kudo A. Sensitization of $NaMO_3$ (M: Nb and Ta) photocatalysts with wide band gaps to visible light by Ir doping. Bull Chem Soc Jpn. 2009 Mar 15;82(4):514–18.
12. Kim HG, Becker OS, Jang JS, Ji SM, Borse PH, Lee JS. A generic method of visible light sensitization for perovskite-related layered oxides: substitution effect of lead. J Solid State Chem. 2006;179(4):1214–18.
13. Konta R, Ishii T, Kato H, Kudo A. Photocatalytic activities of noble metal ion doped $SrTiO_3$ under visible light irradiation. J Phys Chem B. 2004;108(26):8992–95.
14. Nishimoto S, Matsuda M, Miyake M. Photocatalytic activities of Rh-doped $CaTiO_3$ under visible light irradiation. Chem Lett. 2006;35(3):308–9.
15. Sakata Y, Miyoshi Y, Maeda T, Ishikiriyama K, Yamazaki Y, Imamura H, et al. Photocatalytic property of metal ion added $SrTiO_3$ to overall H_2O splitting. Appl Catal Gen. 2016;521:227–32.
16. Zhao Z, Willard EJ, Li H, Wu Z, Castro RHR, Osterloh FE. Aluminum enhances photochemical charge separation in strontium titanate nanocrystal photocatalysts for overall water splitting. J Mater Chem A. 2018;6(33):16170–76.
17. Kato H, Asakura K, Kudo A. Highly efficient water splitting into H_2 and O_2 over lanthanum-doped $NaTaO_3$ photocatalysts with high crystallinity and surface nanostructure. J Am Chem Soc. 2003;125(10):3082–89.
18. Kim J, Hwang DW, Kim HG, Bae SW, Lee JS, Li W, et al. Highly efficient overall water splitting through optimization of preparation and operation conditions of layered perovskite photocatalysts. Top Catal. 2005;35(3):295–303.
19. Shi T, Chen Y, Guo X. Defect chemistry of alkaline earth metal (Sr/Ba) titanates. Prog Mater Sci. 2016;80:77–132.
20. Ham Y, Hisatomi T, Goto Y, Moriya Y, Sakata Y, Yamakata A, et al. Flux-mediated doping of $SrTiO_3$ photocatalysts for efficient overall water splitting. J Mater Chem A. 2016;4(8):3027–33.
21. Goto Y, Hisatomi T, Wang Q, Higashi T, Ishikiriyama K, Maeda T, et al. A particulate photocatalyst water-splitting panel for large-scale solar hydrogen generation. Joule. 2018;2(3):509–20.
22. Zhao Z, Goncalves RV, Barman SK, Willard EJ, Byle E, Perry R, et al. Electronic structure basis for enhanced overall water splitting photocatalysis with aluminum doped $SrTiO_3$ in natural sunlight. Energy Env Sci. 2019;12(4):1385–95.
23. Takata T, Jiang J, Sakata Y, Nakabayashi M, Shibata N, Nandal V, et al. Photocatalytic water splitting with a quantum efficiency of almost unity. Nature. 2020;581(7809):411–14.
24. Zhang M, Guo Z, Gellman AJ, Salvador PA, Rohrer GS. Influence of the molten $SrCl_2$ treatment on the surface structure and photochemical reactivities of $SrTiO_3$. Appl Surf Sci. 2023;638:158111.
25. Higashi T, Seki K, Nandal V, Pihosh Y, Nakabayashi M, Shibata N, et al. Understanding the activation mechanism of $RhCrO_x$ cocatalysts for hydrogen evolution with nanoparticulate electrodes. ACS Appl Mater Interfaces. 2024 May 22;16(20):26325–39.
26. Higashi T, Seki K, Sasaki Y, Pihosh Y, Nandal V, Nakabayashi M, et al. Mechanistic insights into enhanced hydrogen evolution of CrO_x/Rh nanoparticles for photocatalytic water splitting. Chem—Eur J. 2023 Apr 25;29(24):e202204058.
27. Lopato EM, Eikey EA, Simon ZC, Back S, Tran K, Lewis J, et al. Parallelized screening of characterized and DFT-modeled bimetallic colloidal cocatalysts for photocatalytic hydrogen evolution. ACS Catal. 2020 Apr 3;10(7):4244–52.

28. Zhang M, Lopato EM, Ene NN, Funni SD, Du T, Jiang K, et al. Synthesis and structure of an ion-exchanged $SrTiO_3$ photocatalyst with improved reactivity for hydrogen evolution. Adv Mater Interfaces. 2023 Apr 1;10(10):2202476.
29. Dong L, Shi H, Cheng K, Wang Q, Weng W, Han W. Shape-controlled growth of $SrTiO_3$ polyhedral submicro/nanocrystals. Nano Res. 2014 Sep;7(9):1311–18.
30. Zhang M, Salvador PA, Rohrer GS. Influence of particle size and shape on the rate of hydrogen produced by Al-doped $SrTiO_3$ photocatalysts. J Am Ceram Soc. 2022;105(8):5336–46.
31. Dong L, Cheng K, Weng W, Han W. Effect of mineralization agents on the surface structure and dielectric properties of $SrTiO_3$ nanocrystals. CrystEngComm. 2014;16(47):10750–53.
32. Maeda K, Teramura K, Masuda H, Takata T, Saito N, Inoue Y, et al. Efficient overall water splitting under visible-light irradiation on $(Ga_{1-x}Zn_x)(N_{1-x}O_x)$ dispersed with Rh−Cr mixed-oxide nanoparticles: effect of reaction conditions on photocatalytic activity. J Phys Chem B. 2006;110(26):13107–12.
33. Song W, Lopato EM, Bernhard S, Salvador PA, Rohrer GS. High-throughput measurement of the influence of pH on hydrogen production from $BaTiO_3/TiO_2$ core/shell photocatalysts. Appl Catal B Environ. 2020;269:118750.
34. Bowes PC, Ryu GH, Baker JN, Dickey EC, Irving DL. Fermi level pinning in Co-doped $BaTiO_3$: part II. Defect chemistry models. J Am Ceram Soc. 2021;104(11):5859–72.
35. Ryu GH, Bowes PC, McGarrahan JR, Irving DL, Dickey EC. Fermi level pinning in Co-doped $BaTiO_3$: part I. DC and AC electrical conductivities and degradation behavior. J Am Ceram Soc. 2022;105(1):292–98.
36. Brent RP. Algorithms for minimization without derivatives. IEEE Trans Autom Control. 1974;19:632–3.
37. Shin CJ, Yoo HI, Lee CE. Al-doped $SrTiO_3$: part I, anomalous oxygen nonstoichiometry. Solid State Ion. 2007 Jun 1;178(15):1081–87.
38. Mu L, Zhao Y, Li A, Wang S, Wang Z, Yang J, et al. Enhancing charge separation on high symmetry $SrTiO_3$ exposed with anisotropic facets for photocatalytic water splitting. Energy Env Sci. 2016;9(7):2463–69.
39. Lee YG, Cheng YC, Lin YT, Wu JCS, Yu WY, Kržmanc MM, et al. Photocatalytic water splitting of Al-doped $Rh_xCr_{2-x}O_3/SrTiO_3$ synthesized by flux method: elucidating the role of different molten salts. J Phys Chem C. 2023 Jun 1;127(21):9981–91.
40. Puangpetch T, Sreethawong T, Yoshikawa S, Chavadej S. Hydrogen production from photocatalytic water splitting over mesoporous-assembled $SrTiO_3$ nanocrystal-based photocatalysts. J Mol Catal-Chem. 2009 Oct;312(1–2):97–106.
41. Tkach A, Vilarinho PM, Kholkin A. Effect of Mg doping on the structural and dielectric properties of strontium titanate ceramics. Appl Phys A. 2004 Dec 1;79(8):2013–20.
42. Tkach A, Vilarinho PM, Kholkin AL, Pashkin A, Samoukhina P, Pokorny J, et al. Lattice dynamics and dielectric response of Mg-doped $SrTiO_3$ ceramics in a wide frequency range. J Appl Phys. 2005 Jan 24;97(4):044104.
43. Zhang M, Salvador PA, Rohrer GS. Influence of pH and surface orientation on the photochemical reactivity of $SrTiO_3$. ACS Appl Mater Interfaces. 2020 May 20;12(20):23617–26.
44. Shen Q, Kang W, Ma L, Sun Z, Jin B, Li H, et al. Tuning the anisotropic facet of $SrTiO_3$ to promote spatial charge separation for enhancing photocatalytic CO_2 reduction properties. Chem Eng J. 2023;478:147338.
45. Li K, Hao H, Yao Z, Cao M, Liu H. Colossal permittivity and low dielectric loss in (Nb, Ga) co-doped $SrTiO_3$ ceramics sintered in nitrogen atmosphere. Ceram Int. 2024;50(6):8662–68.
46. Zhou X, Toft Sørensen O, Xu Y. Defect structure and oxygen sensing properties of Mg-doped $SrTiO_3$ thick film sensors. Sens Actuators B Chem. 1997;41(1):177–82.
47. Moos R, Hardtl KH. Defect chemistry of donor-doped and undoped strontium titanate ceramics between 1000° and 1400°C. J Am Ceram Soc. 1997;80(10):2549–62.
48. Waser R. Bulk conductivity and defect chemistry of acceptor-doped strontium titanate in the quenched state. J Am Ceram Soc. 1991;74(8):1934–40.
49. Bhardwaj A, Burbure NV, Rohrer GS. Enhanced photochemical reactivity at the ferroelectric phase transition in $Ba_{1-x}Sr_xTiO_3$. J Am Ceram Soc. 2010;93(12):4129–34.
50. Noland JA. Optical absorption of single-crystal strontium titanate. Phys Rev. 1954 May;94(3):724.
51. Albery WJ, Bartlett PN. The transport and kinetics of photogenerated carriers in colloidal semiconductor electrode particles. J Electrochem Soc. 1984 Feb;131(2):315–25.
52. Li L, Salvador PA. Rohrer GS. Photocatalysts with internal electric fields. Nanoscale. 2014;6(1):24–42.
53. Liu M, Lyons JL, Yan D, Hybertsen MS. Semiconductor-based photoelectrochemical water splitting at the limit of very wide depletion region. Adv Funct Mater. 2016;26(2):219–25.
54. Cheng C, Long R. Charge-compensated doping extends carrier lifetimes in $SrTiO_3$ by passivating oxygen vacancy defects. J Phys Chem Lett. 2021 Dec 23;12(50):12040–47.
55. Li R, Takata T, Zhang B, Feng C, Wu Q, Cui C, et al. Criteria for efficient photocatalytic water splitting revealed by studying carrier dynamics in a model Al-doped $SrTiO_3$ photocatalyst. Angew Chem Int Ed. 2023;62(49):e202313537.
56. Han K, Lin YC, Yang CM, Jong R, Mul G, Mei B. Promoting photocatalytic overall water splitting by controlled magnesium incorporation in $SrTiO_3$ photocatalysts. ChemSusChem. 2017;10(22):4510–16.
57. SZh K. Properties of precisely compensated semiconductors. Semiconductors. 2000;34(8):872–9.
58. Zhang M. Enhancing charge separation on metal oxides by space charge engineering for photocatalytic overall water splitting. Carnegie Mellon University; 2022.

SUPPORTING INFORMATION

Additional supporting information can be found online in the Supporting Information section at the end of this article.

How to cite this article: Zhang M, Salvador PA, Rohrer GS. Defect compensation as a strategic approach to enhance photocatalytic water splitting performance of $SrTiO_3$. J Am Ceram Soc. 2026;109:e70296. https://doi.org/10.1111/jace.70296

Supporting information for

Defect compensation as a strategic approach to enhance photocatalytic water splitting performance of $SrTiO_3$

Mingyi Zhang, Paul A. Salvador, Gregory S. Rohrer*

Department of Materials Science and Engineering, Carnegie Mellon University, Pittsburgh, PA 15213, USA

* Corresponding author

E-mail address: gr20@andrew.cmu.edu (G.S. Rohrer)

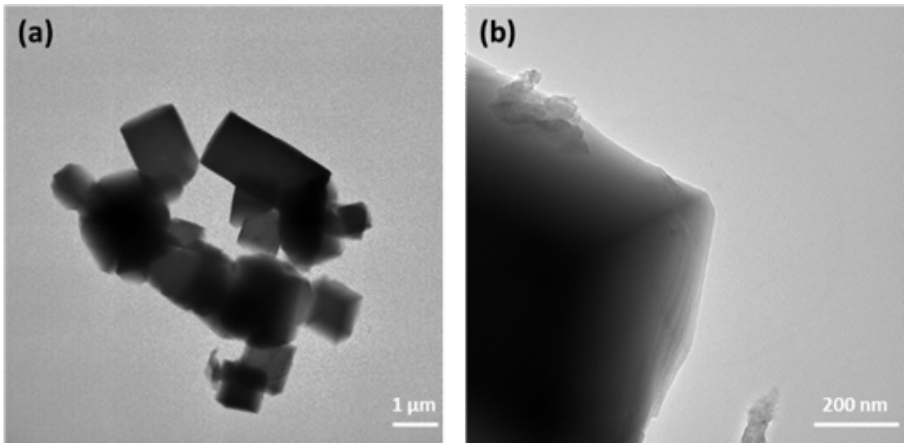

Figure S1: TEM images of undoped $SrTiO_3$ particles after treatment in $SrCl_2$ melt using an alumina crucible.

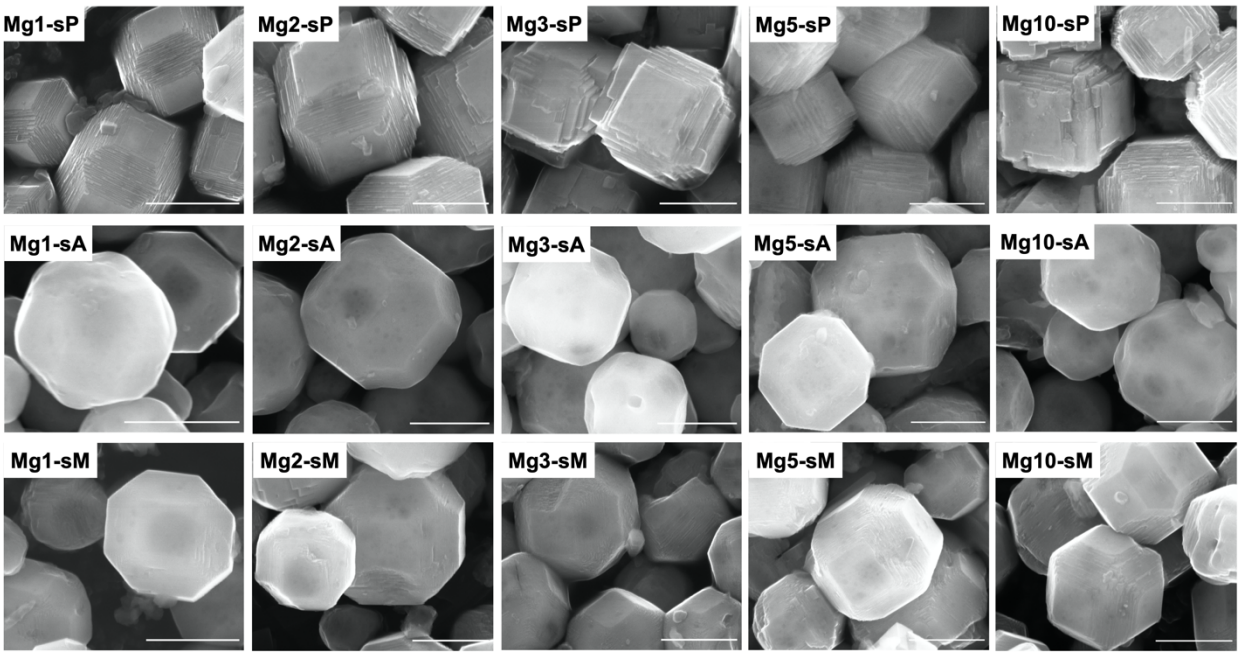

Figure S2: SEM images of Mg-added particles that have been treated in molten $SrCl_2$ in a platinum crucible (-sP), an alumina crucible (-sA) and a magnesia crucible (-sM). The numbers represent Mg dopant additions. The scale bar represents 500 nm.

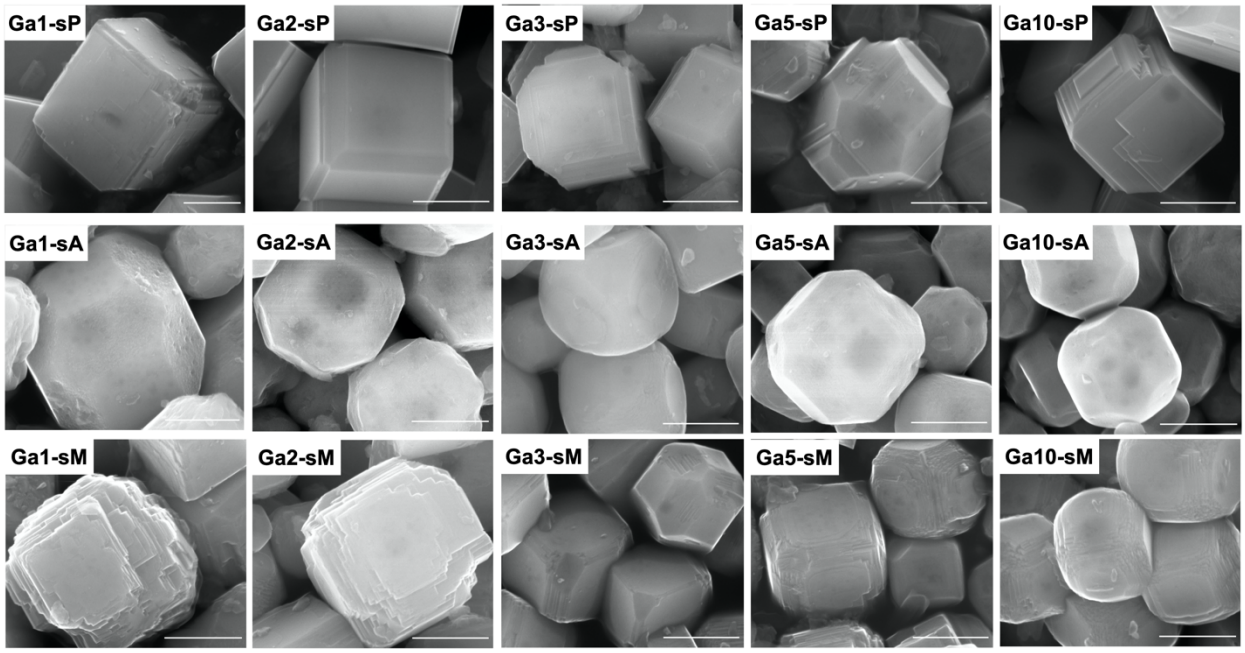

Figure S3: SEM images of Ga-added particles that have been treated in molten $SrCl_2$ in a platinum crucible (-sP), an alumina crucible (-sA) and a magnesia crucible (-sM). The numbers represent Ga dopant additions. The scale bar represents 500 nm.

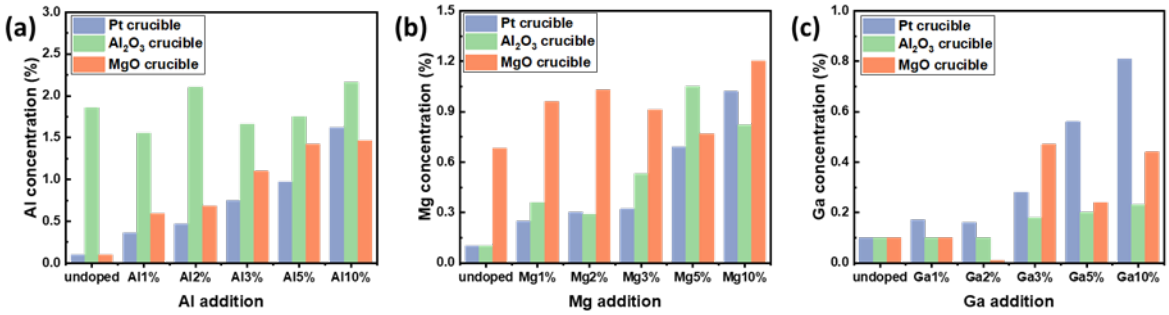

Figure S4: Dopant concentrations measured by EDS for (a) Al-incorporated $SrTiO_3$, (b) Mg-incorporated $SrTiO_3$, and (c) Ga-incorporated $SrTiO_3$.

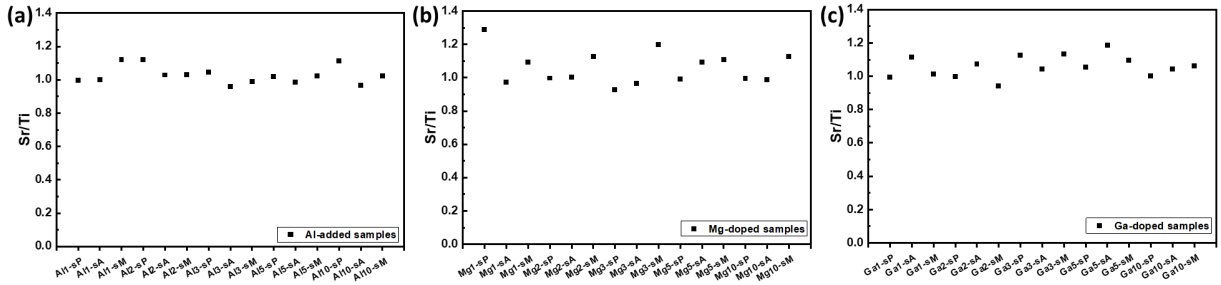

Figure S5: Sr/Ti ratio measured by EDS for (a) Al-incorporated $SrTiO_3$, (b) Mg-incorporated $SrTiO_3$, and (c) Ga-incorporated $SrTiO_3$.

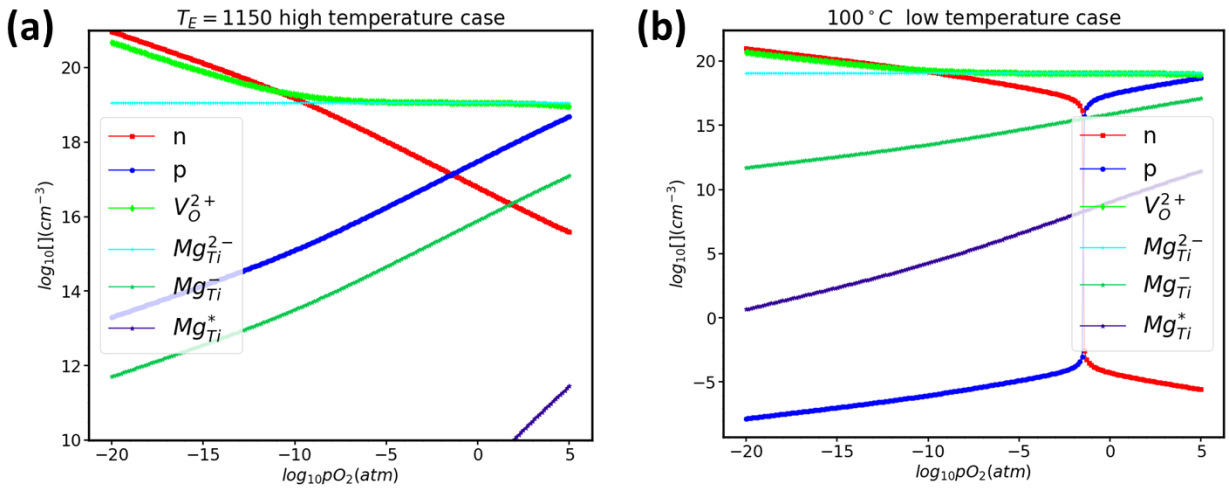

Figure S6: Brouwer diagrams of 0.07% Mg-doped $SrTiO_3$ at 1150 °C and 100 °C. In the absence of reported quantitative data for the mass action constants, we assume the first ionization energy for Mg is the same as in the Al-doped case, and the second ionization energy is four times greater, based on hydrogenic model considerations. The simulation results show that the oxygen partial pressure at which n=p shifts to lower values (leftward), consistent with enhanced compensation by Mg doping.

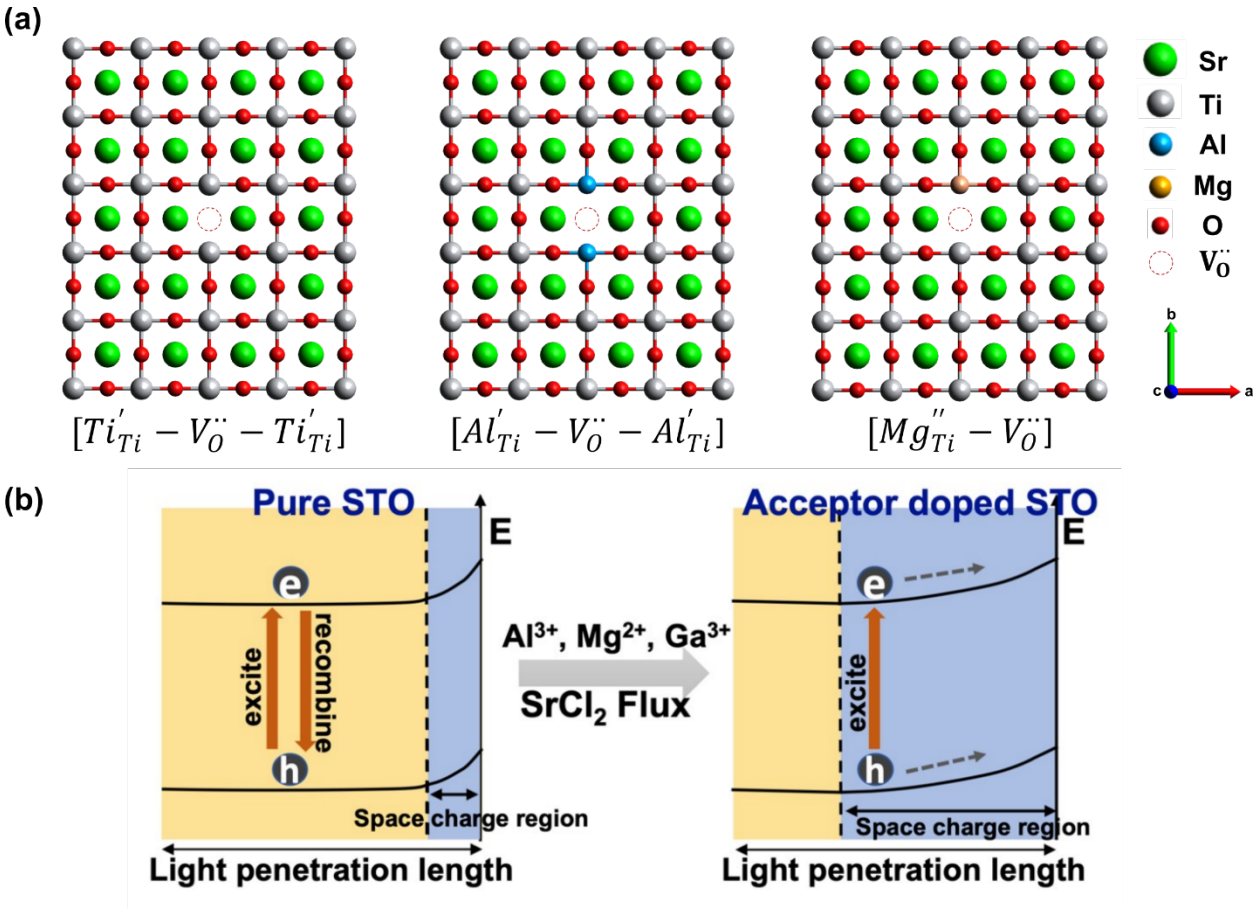

Figure S7: (a) Crystal structures of vacancy doped $SrTiO_3$, Al-doped $SrTiO_3$, and Mg-doped $SrTiO_3$. (b) Schematic illustration of how the incorporation of Al^{3+}, Mg^{2+} and Ga^{3+} influences the space charge region of $SrTiO_3$.

Table S1: Molar ratios of the 15 hydrothermally doped $SrTiO_3$ crystals estimated from the data in Table 1. These crystals were not treated in a $SrCl_2$ melt.

Sample	$\frac{\textbf{Al\%}}{\textbf{Al\% + Ti\%}}$	**Sample**	$\frac{\textbf{Mg\%}}{\textbf{Mg\% + Ti\%}}$	**Sample**	$\frac{\textbf{Ga\%}}{\textbf{Ga\% + Ti\%}}$
Al1	0.044%	Mg1	0.24%	Ga1	0.12%
Al2	0.088%	Mg2	0.63%	Ga2	0.24%
Al3	0.13%	Mg3	1.01%	Ga3	0.36%
Al5	0.22%	Mg5	1.49%	Ga5	0.60%
Al10	0.44%	Mg10	2.98%	Ga10	1.2%